Revista Internacional de Métodos Numéricos para Cálculo y Diseño en Ingeniería

Tech Science Press

https://doi.org/10.32604/rimni.2026.082533

ARTICLE

Iber1D: A Computational Framework for Junction and Boundary Modeling in Open-Channel Networks

Danial Dehghan-Souraki*, Marcos Sanz-Ramos and Ernest Bladé i Castellet

Flumen Institute, Universitat Politècnica de Catalunya (UPC-Barcelona TECH)-International Centre of Numerical Methods in Engineering (CIMNE), Barcelona, Spain

*Corresponding Author: Danial Dehghan-Souraki. Email: danial.dehghan@upc.edu

Received: 17 March 2026; Accepted: 03 June 2026; Published: 06 November 2026

ABSTRACT: Simulating unsteady flow in open channel networks requires balancing computational efficiency with physical accuracy, particularly at junctions where one-dimensional (1D) Saint-Venant equations are invalid. This paper presents Iber1D, a novel hybrid model integrating a 1D finite volume solver with Roe's approximate Riemann scheme for channel reaches and a physics-based two-dimensional (2D) formulation for junctions. Junctions are treated as storage volumes with rigorous mass and momentum conservation, while hydraulic structures (gates and weirs) are modeled as internal boundary conditions. The model was validated against the established Iber 2D shallow water solver across gradually varied flow profiles (M and S curves), hydraulic jumps, flow regime transitions, and complex multi-reach networks. Results demonstrate excellent agreement with the 2D reference for macroscopic variables (water depths and boundary discharges). While the 1D formulation inherently averages out localized intra-junction eddies, it successfully resolves the aggregate flow distribution through confluences and bifurcations. The proposed approach provides a computationally efficient tool for flood forecasting, irrigation network management, and urban drainage analysis.

KEYWORDS: 1D hydrodynamic modeling; Saint-Venant equations; channel networks; junction modeling; finite volume method; Roe solver

1 Introduction

The management of water resources in engineered and natural channel networks has transitioned to a predictive, simulation-driven approach, which is now essential for predictive flood risk assessment [1–3], real-time operational control [4,5], and long-term strategic planning [6]. This evolution is driven by specific hydrological mechanisms, such as flow regime responses to increased imperviousness in urbanized landscapes [7,8], alongside the shifting frequency and intensity of extreme precipitation events, which collectively intensify complex hydraulic challenges [9–12]. Urban drainage systems, for example, require sophisticated "dual drainage" models to accurately simulate pluvial flooding, manhole overflows, and combined sewer overflows (CSOs) [13–17]. Concurrently, agricultural networks depend on robust modeling to optimize water allocation for global food security [18,19] and to manage pervasive issues like sediment transport [20,21], aquatic vegetation growth [22,23], and the cumulative hydrological impacts of numerous small-scale structures [24,25]. A fundamental tension exists between the physical realism of computationally expensive multi-dimensional models and the efficiency of simplified traditional 1D models [26–28].

The choice of model dimensionality in any hydraulic study represents a fundamental trade-off between computational cost and the required physical realism. One-dimensional (1D) models, which solve the

Copyright © 2027 The Authors. Published by Tech Science Press. This work is licensed under a Creative Commons Attribution 4.0 International License, which permits unrestricted use, distribution, and reproduction in any medium, provided the original work is properly cited.

Saint-Venant equations averaged over discrete cross-sections, are exceptionally efficient [29–31]. This makes them ideal for simulating large-scale networks, conducting long-term continuous simulations [32,33], and handling hydraulic structures, for which they often have mature, robust modules [34,35]. Their primary limitation, however, is an inherent inability to simulate lateral or multi-directional flow, rendering them unsuitable for complex floodplains. Conversely, two-dimensional (2D) models solve the depth-averaged shallow water equations over a continuous mesh [36–38], providing physically realistic, detailed spatial maps of water depth and velocity, which is critical for understanding complex, multi-directional flow in urban areas or overbanks [39,40]. This accuracy comes at the cost of being computationally expensive and requiring high-resolution topographic and bathymetric data—typically defined as sub-meter grid resolutions or mesh elements significantly finer than the channel width [41]. Furthermore, acquiring this data introduces significant collection trade-offs [42]. While Terrestrial Laser Scanning (TLS) provides the necessary sub-centimeter topographical precision, it is highly labor-intensive to execute over large river reaches. Conversely, while standard Unmanned Aerial Vehicle (UAV) LiDAR is highly efficient for wide-area floodplain mapping, its near-infrared pulses cannot penetrate the water surface to capture the accurate sub-aqueous bathymetry essential for 2D modeling. As a pragmatic compromise, coupled 1D-2D models have emerged, using 1D for the efficient simulation of the main channel and 2D for the accurate representation of adjacent floodplains [43–45]. While this hybrid approach offers an optimal balance for many riverine flood studies, its overall accuracy is highly dependent on the complex formulation of the 1D-2D coupling interface [46]. A summary of primary hydrodynamic modeling approaches is presented in Table S1 (Supplementary Material).

For any 1D model applied to a network, the treatment of channel junctions represents the single greatest challenge and the most significant potential source of error. The 1D Saint-Venant equations are not valid at the junction itself, which must instead be treated as a complex internal boundary condition [47,48]. A junction is not a simple, zero-dimensional point but a complex hydrodynamic zone where the fundamental assumptions of 1D flow—such as unidirectional, parallel streamlines—break down completely [48]. In confluences, the merging of flows with different momentum vectors creates shear layers, flow separation from boundaries, and large-scale turbulent recirculation [49–52]. These processes induce significant, localized energy losses that are not accounted for by standard 1D bed friction formulas. Similarly, in a diffluence where flow divides, the geometry forces rapid changes in flow direction, leading to water surface superelevation and complex secondary currents [53]. This flow behavior is inherently two- or even three-dimensional, and accurately modeling its effect on energy dissipation and flow distribution is critical for the simulation of the entire network [45,53].

The treatment of hydraulic junctions in network models has evolved through several paradigms with progressively increasing physical rigor (Table S2 (Supplementary Material)). The simplest and most widespread approach is the *equal-level node* model, as implemented in widely used software such as the EPA Storm Water Management Model (SWMM) [54]. In this framework, the junction is treated as a zero-dimensional point where only mass conservation is enforced, assuming a uniform water surface elevation across the node and at the proximal ends of all connected conduits. While computationally efficient, this approach neglects momentum conservation entirely: the transition at the node is essentially a transformation of kinetic energy into potential energy, ignoring directional changes of the flow and the internal turbulence generated by merging or dividing streams. This leads to inaccuracies in the energy grade line prediction, particularly in high-velocity flows where directional momentum changes are significant.

A second paradigm addresses junction energy losses through *empirical loss coefficients* (K), which relate the head loss to the velocity head via $\Delta h = Kv^2/2g$ [55,56]. These coefficients depend on the Reynolds number, discharge ratios, junction geometry, and flow regime, and their determination typically requires extensive experimental data or three-dimensional CFD modeling. While this approach corrects the energy

grade line, it remains a descriptive rather than predictive method: the K-factors are regime-dependent, often unavailable for irregular geometries encountered in practice, and may create numerical discontinuities during flow reversal—making them a mandatory yet uncertain input for dynamic simulations.

More physically based formulations have sought to resolve the junction physics directly. The Junction Riemann Problem (JRP) treats junctions as discontinuities in the 1D domain and solves a generalized Riemann problem for the resulting wave patterns, providing robust solutions across flow regimes without empirical coefficients [57]. Alternatively, the integrated 1D-2D coupling approach, notably developed by Ghostine et al. [48], discretizes the junction as a *fully resolved* two-dimensional mesh, solving the shallow water equations on a fine grid within the junction area. This permits explicit computation of 2D flow dynamics, including flow separation, recirculation zones, and internal shock waves [58]. However, the requirement for a detailed junction mesh significantly increases the computational cost and mesh generation complexity, limiting the scalability of this approach for large-scale network simulations with numerous junctions.

The global objective of this work is to develop and validate a robust 1D hydrodynamic module integrated within the Iber software suite [37], addressing the need for efficient yet physically accurate network simulations. In contrast to the existing approaches summarized in Table S2 (Supplementary Material), the proposed model introduces the following specific contributions: (i) a control-volume-based junction formulation that conserves both mass and two-dimensional momentum without requiring a resolved 2D mesh at the junction, deriving energy dissipation as an emergent property of the momentum balance rather than relying on pre-defined empirical coefficients; (ii) the use of Roe's approximate Riemann solver at both the 1D channel interfaces and the 1D-2D junction boundaries, ensuring numerical consistency and flux continuity across domains; (iii) the inclusion of a hydrostatic wall thrust term ($\mathbf{S}_{wall}$) that accounts for the reaction forces exerted by the physical boundaries of the junction on the flow, providing a physical mechanism for head losses at junctions with finite area without empirical calibration; and (iv) full integration within the Iber software suite, enabling large-scale network simulations with the enhanced junction physics at practical computational costs. By validating this complete model against the established Iber 2D shallow water solver, this work demonstrates that the proposed approach achieves routing accuracy comparable to fully resolved 2D simulations at a fraction of the computational cost.

2 Materials and Methods

This section details the mathematical formulation and numerical implementation of the developed one-dimensional (1D) hydrodynamic model. The model is designed to simulate unsteady free-surface flow in complex channel networks, employing a robust finite volume framework that ensures conservation of mass and momentum both along the channels and at their junctions.

2.1 Hydrodynamic Module

The core of the model solves the one-dimensional Saint-Venant equations [59,60], which describe the conservation of mass and momentum for unsteady open channel flow. These equations are expressed in their conservative vector form as:

$$\frac{\partial \mathbf{U}}{\partial t} + \frac{\partial \mathbf{F}(\mathbf{U})}{\partial x} = \mathbf{H}(\mathbf{U}) \tag{1}$$

where t represents time, x is the longitudinal spatial coordinate, $\mathbf{U}$ is the vector of conserved variables, $\mathbf{F}$ is the flux vector, and $\mathbf{H}$ is the source term vector. These are defined as:

$$\mathbf{U} = \begin{pmatrix} A \\ Q \end{pmatrix}, \quad \mathbf{F} = \begin{pmatrix} Q \\ \frac{Q^2}{A} + I_1 \end{pmatrix}, \quad \mathbf{H} = \begin{pmatrix} 0 \\ gA(S_0 - S_f) + I_2 \end{pmatrix} \tag{2}$$

Here, A represents the wetted cross-sectional area, Q is the discharge, g is the acceleration due to gravity, S_0 is the bed slope, and S_f is the friction slope calculated using Manning's formula:

$$S_f = \frac{n^2 Q|Q|}{A^2 R_h^{4/3}} \tag{3}$$

where n is Manning's roughness coefficient and R_h is the hydraulic radius.

The terms I_1 and I_2 represent the hydrostatic pressure force integral and the pressure force component due to longitudinal variations in channel width, respectively. They are formulated to account for arbitrary cross-sectional shapes:

$$I_1 = \int_0^h (h - \eta)\sigma(x, \eta) d\eta \tag{4}$$

$$I_2 = \int_0^h (h - \eta)\frac{\partial \sigma(x, \eta)}{\partial x} d\eta \tag{5}$$

where h is the water depth, η is the vertical integration variable, and $\sigma(x, \eta)$ is the channel width at elevation η.

Numerical Scheme

The detailed numerical discretization, explicit integration scheme, C-property preservation, and Roe's approximate Riemann solver for the 1D reaches are presented in Section S1 of the Supplementary Material.

2.2 Junctions

A critical component of the model is its capability to simulate complex channel networks where multiple reaches converge or diverge [59]. The implementation treats junctions as distinct nodal elements that connect the boundaries of the adjacent 1D channel segments.

2.2.1 Junction Model Formulation

The junction is modeled as a 2D horizontal storage volume Ω_J where both mass and momentum conservation are enforced. Unlike simple point-node approximations, this model accounts for the finite surface area of the junction and its physical boundaries. The spatial discretization of the junction and its connection to 1D channels is illustrated in Fig. 1.

Let $\mathbf{U}_J = [h_J, h_J u_J, h_J v_J]^T$ be the 3×1 state vector representing the water depth and the unit-width momentum components in the x and y directions within the junction. For a junction J connected to N_c 1D channels, the integral form of the balance equations over the junction domain yields:

$$\frac{\partial \mathbf{U}_J}{\partial t}\Omega_J + \sum_{k=1}^{N_c} \mathbf{\Phi}^*_{k,J} \Delta w_k = \mathbf{S}_J + \mathbf{S}_{wall} \tag{6}$$

where Δw_k is the width of the interface connecting channel k to the junction. To properly couple the 1D channels with the 2D junction dynamics, $\mathbf{\Phi}^*_{k,J}$ is defined as a 3×1 numerical flux vector representing the projection of the 1D fluxes into the 2D coordinate system of the junction:

$$\mathbf{\Phi}^*_{k,J} = \begin{pmatrix} F^*_{mass,k} \\ F^*_{mom,k} n_{x,k} \\ F^*_{mom,k} n_{y,k} \end{pmatrix} \tag{7}$$

Here, $F^*_{mass,k}$ and $F^*_{mom,k}$ are the scalar mass and momentum fluxes computed by the 1D Roe solver at interface k, and $\mathbf{n}_k = (n_{x,k}, n_{y,k})^T$ is the outward unit normal vector of the interface k pointing out of the junction.

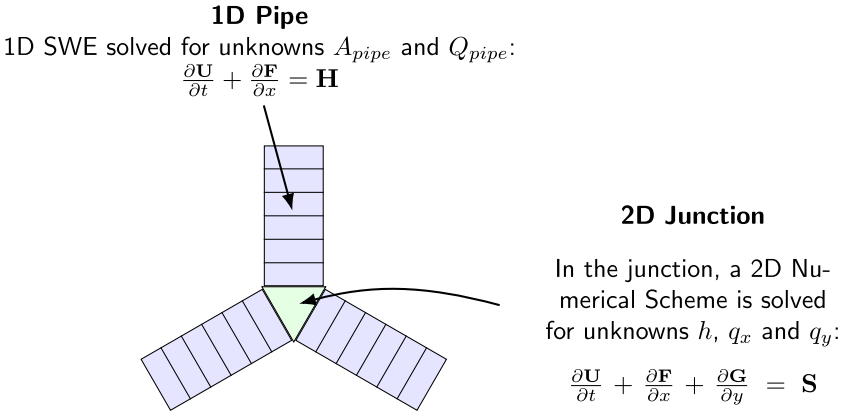


Figure 1: Schematic representation of the spatial discretization: 1D channels connected to a 2D junction domain.

The term $\mathbf{S}_J$ contains internal source terms (e.g., bed friction and external mass inflows). Crucially, the term $\mathbf{S}_{wall}$ represents the hydrostatic thrust acting on the solid, impermeable walls of the junction (i.e., the portions of the junction perimeter Γ_{wall} not connected to any channel). It is formulated as:

$$\mathbf{S}_{wall} = \begin{pmatrix} 0 \\ \int_{\Gamma_{wall}} I_1 n_x dl \\ \int_{\Gamma_{wall}} I_1 n_y dl \end{pmatrix} \tag{8}$$

If the junction is conceptualized purely as a point-node connecting pipes without physical solid walls (where all edges are inflow or outflow boundaries), $\mathbf{S}_{wall}$ is explicitly zero. However, for junctions with finite areas and defined solid boundaries, excluding this hydrostatic thrust would result in an unphysical momentum imbalance.

2.2.2 Numerical Treatment of Junctions

The numerical treatment, flux projection, Roe solver application at the interfaces, and the time-stepping updates for the junctions are detailed in Section S2 of the Supplementary Material.

2.3 Boundary Conditions

The numerical treatment of boundary conditions is based on the method of characteristics and the ghost cell approach. The model supports inlet, outlet, and internal boundary conditions.

2.3.1 Inlet and Outlet Boundaries

At the inlet and outlet, the number of physical conditions to be imposed depends on the flow regime (subcritical or supercritical), determined by the Froude number Fr.

- Subcritical Inlet ($Fr < 1$): One physical condition is required. Typically, the discharge $Q(t)$ is imposed. The water-level in the ghost cell is extrapolated from the interior domain (zero-order extrapolation $h_{ghost} \approx h_{internal}$) or computed using the backward Riemann invariant $J^- = u - 2c$ [61].
- Supercritical Inlet ($Fr > 1$): Two physical conditions are required. Both discharge $Q(t)$ and water-level $h(t)$ (or energy head) must be imposed.
- Subcritical Outlet ($Fr < 1$): One physical condition is required, such as a fixed water-level $h(t)$ or a rating curve $Q(h)$. For a free overfall, the critical depth condition is imposed if the flow attempts to become supercritical at the boundary: $h_{ghost} = \max(h_{internal}, h_c)$.
- Supercritical Outlet ($Fr > 1$): No physical conditions are required. All flow variables are extrapolated from the interior domain (transmissive boundary).

2.3.2 Internal Conditions

Hydraulic structures like gates and weirs are modeled as internal singularities where the standard momentum equation is replaced by specific discharge laws [60].

Gates: The flow through a gate is calculated based on the gate opening h_g and the upstream (H_u) and downstream (H_d) heads.

- Free Flow: When the downstream level is low ($H_d < z_{gate} + \frac{2}{3}h_g$), the discharge is:

$$Q = C_d b h_g \sqrt{2g(H_u - z_{gate})} \tag{9}$$

- Submerged Flow: When the gate is submerged ($H_d > z_{gate} + \frac{4}{5}h_g$):

$$Q = C_{d,sub} b h_g \sqrt{2g(H_u - H_d)} \tag{10}$$

- Transition Flow: For intermediate conditions, a transition formula is applied:

$$Q = C_d b h_g \sqrt{6g(H_u - H_d)} \tag{11}$$

Weirs: Flow over a sharp-crested weir is modeled using the Poleni formula [60] and a Villemonte-type correction for submergence [62].

- Free Flow:

$$Q = C_w L (H_u - z_w)^{1.5} \tag{12}$$

- Submerged Flow:

$$Q = C_w L \frac{3\sqrt{3}}{2} \sqrt{H_u - H_d}(H_d - z_w) \tag{13}$$

where $C_d, C_{d,sub}, C_w$ are discharge coefficients, b and L are the width of the gate and weir, respectively, and z_{gate}, z_w are the sill elevations.

Flux Limiter: This internal boundary allows the user to define a maximum discharge threshold, Q_{max}. The model enforces this constraint by limiting the flow through the cross-section:

$$Q = \begin{cases} Q_{computed} & \text{if } |Q_{computed}| \leq Q_{max} \\ Q_{max} \cdot \text{sgn}(Q_{computed}) & \text{if } |Q_{computed}| > Q_{max} \end{cases} \quad (14)$$

where $Q_{computed}$ is the discharge calculated by the Riemann solver before the limitation is applied.

3 Validation

The newly developed 1D hydrodynamic module has been systematically validated against the previously implemented and widely tested 2D module of Iber, which has been extensively applied from fundamental open-channel hydrodynamics [37,63–65] to complex eco-hydraulics and urban hydrology [66–68]. The latter has already been employed in numerous applications involving both simple and complex channel geometries, and therefore serves as a robust reference for comparison. The validation has been carried out under a variety of flow conditions and geometric configurations that are representative of phenomena typically observed in open channel networks. In all cases, the results of the 1D model show excellent agreement with those of the 2D model, confirming its reliability.

3.1 Hydrodynamics

The following test cases illustrate the model's performance in simulating key hydraulic phenomena, including backwater curves, gradually varied flow profiles on moderate and steep slopes, transitions between flow regimes, and local phenomena around structures and bed forms. Table 1 synthesizes the ID and main characteristics of the models simulated, the ID describing the kind of flow regime (GVF: gradually varied flow; RVF: rapidly varied flow; LP: local phenomenon). Both 1D and 2D models discretized the computational domain using one-dimensional elements with the same variable width and a length of 1 m, making the results directly comparable.

Table 1: ID and main characteristics of the hydrodynamics test cases.

ID	Main Characteristics
GVF_M1a	Backwater curve (M1)
GVF_M1b	Backwater curve (M1)
GVF_M2a	Backwater curve (M2)
GVF_M2b	Backwater curve (M2)
GVF/RVF_M3a	Backwater curve (M3) and 1 hydraulic jump
GVF/RVF_M3M2a	Backwater curves (M3, M2) and 1 hydraulic jump
GVF/RVF_M3M2b	Backwater curves (M3, M2) and 1 hydraulic jump
GVF/RVF_S1a	Backwater curve (S1) and 1 hydraulic jump
GVF/RVF_S1b	Backwater curve (S1) and 1 hydraulic jump
GVF_S3a	Backwater curve (S3)
GVF_S3b	Backwater curve (S3)
GVF_M2S2	Backwater curves (M2, S2)
GVF/RVF_M2S2	Backwater curves (M2, S2) and 1 hydraulic jump
GVF/RVF_S2S1M2	Backwater curves (S2, S2, M2) and 1 hydraulic jump
GVF/RVF_S3S1M2	Backwater curves (S3, S2, M2) and 1 hydraulic jump
LP_1	Local phenomenon (stair) and backwater curve (M2)
LP_2	Local phenomenon (stair) and backwater curve (M1)
LP_3	Local phenomenon (stair) and backwater curves (M1, M2, M2) and 1 hydraulic jump
LP_4	Local phenomenon (stair) and backwater curves (S2, S2) and 1 hydraulic jump
LP_5	2 local phenomena (narrowing, stair), 1 hydraulic jump and, backwater curves (M1, M2)

A comprehensive validation is performed for various Gradually Varied Flow (GVF) profiles on moderate slopes, where normal depth is greater than critical depth ($y_n > y_c$). The simulations reproduce the experimental setup of a rectangular channel with length L = 200 m, width B = 0.5 m, slope S_0 = 0.002, and Manning's roughness n = 0.015 s/m$^{1/3}$ [64]. This configuration allows for the generation of three distinct backwater curves by varying the boundary conditions as summarized in Table 2: the M1 and M2 profiles, which occur in the subcritical regime, and the M3 profile, which occurs in the supercritical regime. The results presented in Fig. 2 show excellent agreement between the 1D and 2D models across all test cases, justifying the use of the computationally efficient 1D model for a wide range of practical engineering problems on such slopes. This set of tests confirms the model's capability to reproduce all three M-curve profiles:

- **M1 profiles** (subplots a, b): These represent classic backwater curves where the flow depth is above the normal depth ($y > y_n > y_c$). This condition is typically caused by a downstream obstruction, such as a dam or weir, which forces the water level to rise. The flow is subcritical and decelerating in the upstream direction. The near-perfect match between the 1D and 2D results indicates that, for this type of gradually varied, subcritical flow, the cross-sectional velocity distribution is sufficiently uniform that a one-dimensional approach is sufficient to capture the flow physics accurately.
- **M2 profiles** (subplots c, d): These are drawdown curves where the flow depth is between the normal and critical depths ($y_n > y > y_c$). This profile occurs as subcritical flow accelerates towards a downstream control point, such as a free overfall or a transition to a steeper channel slope. The ability of the 1D model to precisely replicate the 2D simulation validates its performance in handling accelerating subcritical flows and predicting the water surface as it approaches a critical flow condition.
- **M3 profiles** (subplots e, f, g): These profiles are formed when supercritical flow ($y < y_c < y_n$) enters a moderate slope, a condition which is inherently unstable. The moderate slope cannot sustain the high velocity, causing the flow depth to increase. This increase continues until the flow abruptly transitions to its stable subcritical state through a hydraulic jump, a region of rapidly varied flow with significant energy dissipation. The fact that the 1D model accurately captures the location and the sharp rise in water level of the hydraulic jump is a critical validation of its shock-capturing capabilities and its formulation for energy loss in such discontinuous flows. The minor discrepancies observed between the 1D and 2D results in subfigure (g)—specifically regarding the exact steepness and spatial extent of the jump's face—stem from differences in cross-sectional momentum distribution [69]. The fully 2D model inherently captures lateral velocity gradients and two-dimensional wave reflections, leading to a slightly diffused transition. Conversely, the 1D model averages the momentum over the cross-section (implicitly assuming a uniform velocity distribution with a Boussinesq coefficient $\beta = 1$), causing the Riemann solver to capture the hydraulic jump as a sharper, idealized discontinuity [70].

Table 2: Boundary conditions and hydraulic parameters for the moderate slope GVF profiles.

Curve	Inlet Q (m^3/s)	Inlet v (m/s)	Outlet Condition	y_n (m)	y_c (m)
M1	0.04	–	Level = 0.4 m	0.135	0.087
M2	0.50	–	Critical	0.980	0.470
M3	0.50	15	Critical	0.980	0.470

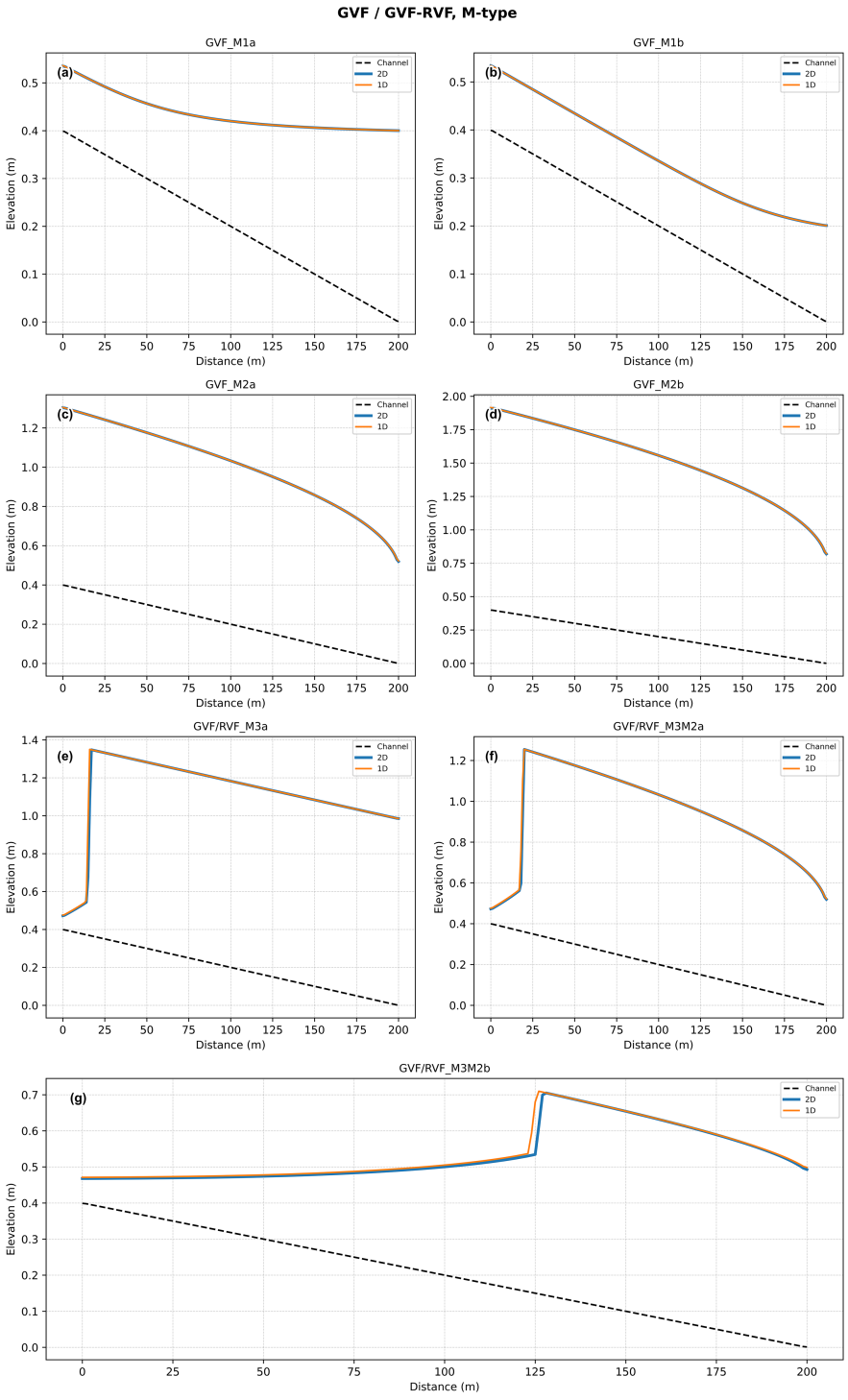


Figure 2: Comparison of 1D and 2D results for test-case group ID GVF_GVFRVF_M-type. Subfigures correspond to: (**a**,**b**) Water depth and flow variables for the M1 profile; (**c**,**d**) for the M2 profile; and (**e**–**g**) for the M3 profile, including the hydraulic jump.

Similarly, the model is validated for steep slope conditions ($y_n < y_c$ and $S_0 = 0.05$), where the normal depth is less than the critical depth, and the flow is predominantly supercritical. The geometry is otherwise identical to the moderate slope case (L = 200 m, B = 0.5 m, n = 0.015 s/m$^{1/3}$). By modifying the boundary conditions as summarized in Table 3, the model reproduces the S1, S2, and S3 profiles. The S1 and S2 curves are generated with a downstream level imposition, while the S3 curve represents a supercritical flow transition. The results in Fig. 3 confirm that the 1D model accurately reproduces all three S-curve profiles, correctly predicting the water surface elevation from the downstream boundary condition (S1, S2) and the supercritical inlet condition (S3), in close agreement with the 2D reference.

Table 3: Boundary conditions and hydraulic parameters for the steep slope GVF profiles.

Curve	Inlet Q (m^3/s)	Inlet v (m/s)	Outlet Condition	y_n (m)	y_c (m)
S1, S2	1.0	2.70	Level = 8 m	0.45	0.74
S3	1.0	20	Critical	0.45	0.74

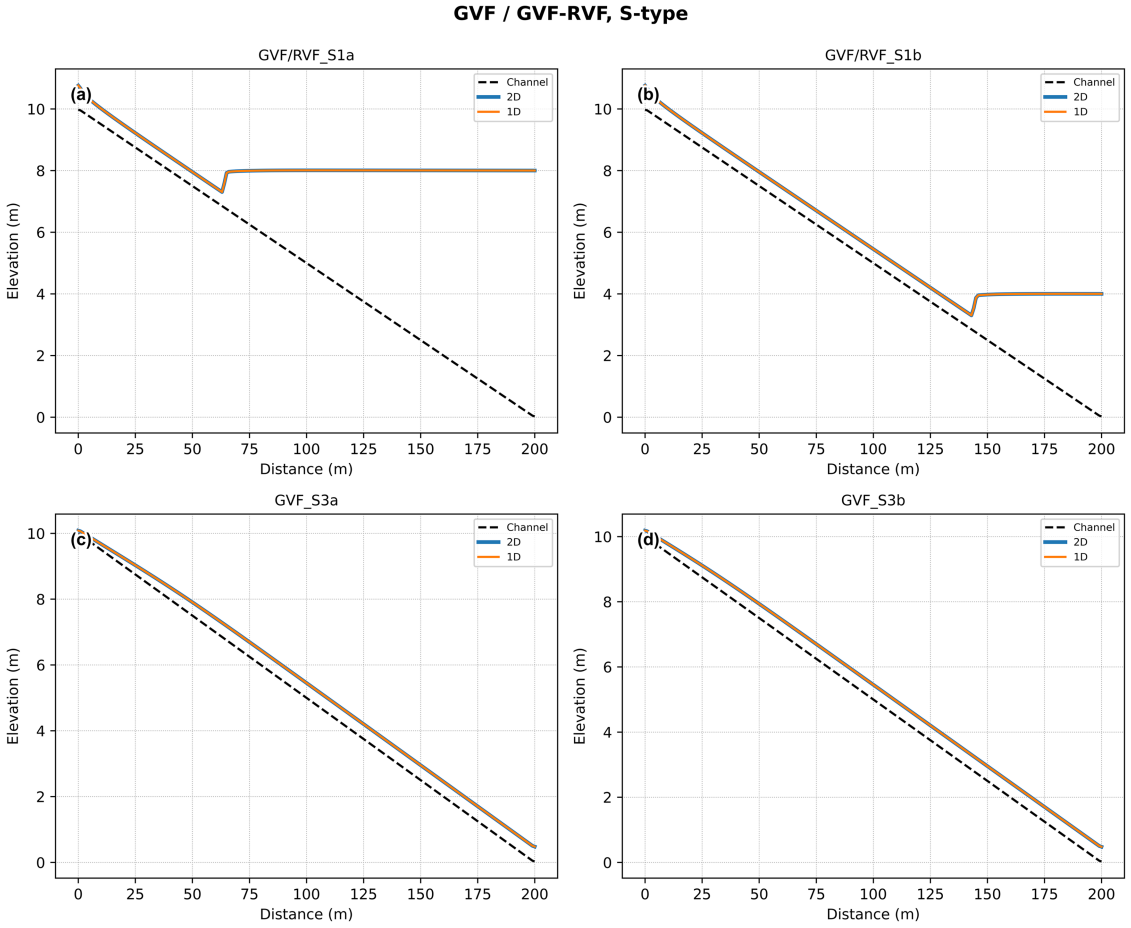


Figure 3: Comparison of 1D and 2D results for test-case group ID GVF_GVFRVF_S-type. Subfigures correspond to: (**a**,**b**) S1 and S2 profiles; (**c**,**d**) S3 profile.

The tests include:

- **S1 and S2 profiles** (subplots a, b): A backed-up water surface profile on a steep slope, forced by a downstream subcritical condition, which terminates in a hydraulic jump.
- **S3 profiles** (subplots c, d): A profile where flow entering at a depth below normal depth accelerates and gradually approaches y_n.

A crucial aspect of hydrodynamic modeling is the ability to handle transitions between flow regimes. The geometry for these cases, depicted in Fig. S1 (Supplementary Material), consists of two connected 200 m reaches with a width of 0.5 m. Subplots (a) and (b) show the transition from a moderate (S_0 = 0.002) to a steep (S_0 = 0.05) slope, where the model accurately captures the passage of the flow through the critical depth at the break in grade. Conversely, subplots (c) and (d) show the transition from a steep to a moderate slope, where the model correctly predicts the formation of a hydraulic jump to dissipate energy and establish subcritical flow. The corresponding results in Fig. 4 validate the model for these scenarios.

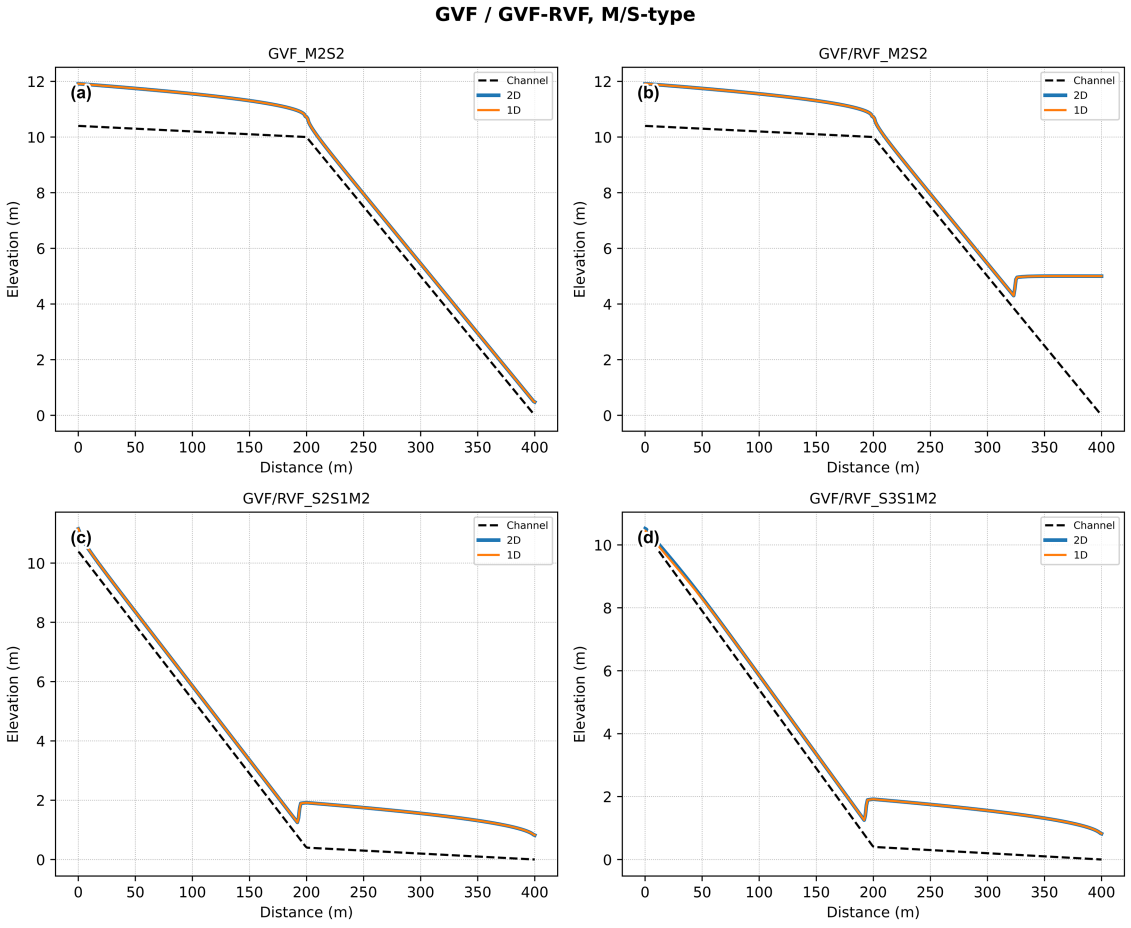


Figure 4: Comparison of 1D and 2D results for test-case group ID GVF_GVFRVF_MS-type. Subfigures correspond to: (**a**,**b**) transition from a moderate to a steep slope; (**c**,**d**) transition from a steep to a moderate slope.

As a final GVF/RVF benchmark before the local-phenomena cases, the model's ability to simulate backwater curves over a complex, multi-sloped channel bed is assessed. The geometry, illustrated in Fig. S2 (Supplementary Material), consists of a 10 m wide rectangular channel (B = 10 m) with a constant Manning's roughness of n = 0.015 s/m$^{1/3}$. The channel is divided into four 500 m reaches with slopes of 0.001, 0.02,

0.06, and 0.001, respectively. This profile, typical of subcritical flow, is caused by a downstream control that raises the water surface elevation above the normal depth. The results in Fig. 5 show that the 1D model perfectly reproduces the smooth water surface profile predicted by the 2D model, demonstrating its accuracy in capturing the upstream propagation of downstream boundary conditions.

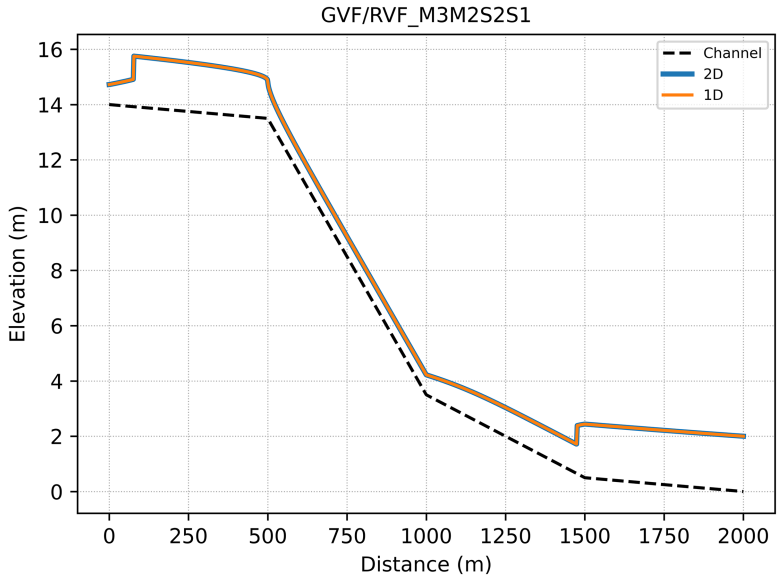


Figure 5: Comparison of 1D and 2D results for a backwater curve.

Finally, the model's performance in resolving local phenomena is assessed, with the case definitions adapted from Gómez et al. [64]. The detailed geometries for IDs LP_1 to LP_4 are presented in Fig. S3 (Supplementary Material). Fig. 6 then demonstrates the corresponding response of flow to small-scale bed forms in rectangular channels (B = 5 m, n = 0.015) under varying regimes.

Panel (a) depicts a channel with a moderate slope where the bed rises abruptly in a long step (Δy = 0.04 m) under subcritical flow. Panel (b) introduces a short-length step (10 m long) where the bed rises and immediately descends. Panel (c) examines a similar geometry with a free discharge outlet downstream. Panel (d) presents a steep channel in a supercritical regime interacting with a significant bed rise (Δy = 0.50 m). As predicted by energy conservation principles, the water surface in the subcritical scenarios dips over the crest of the humps as velocity increases, while the supercritical case captures the necessary hydraulic transitions.

For ID LP_5, the geometry is first presented in Fig. S4 (Supplementary Material). This complex, composite channel profile includes variable widths (B_1 = 10 m, B_2 = B_3 = 8 m) and slopes (1%, 0.12%, 0.12%) with a central step of Δy = 0.40 m and reach lengths sufficient to observe asymptotic trends. The corresponding results in Fig. 7 show that this single case successfully simulates a sequence of phenomena: supercritical flow on an initial steep reach, a forced hydraulic jump caused by a sill, subcritical flow over a flat section, and a subsequent transition back to supercritical flow at a channel drop.

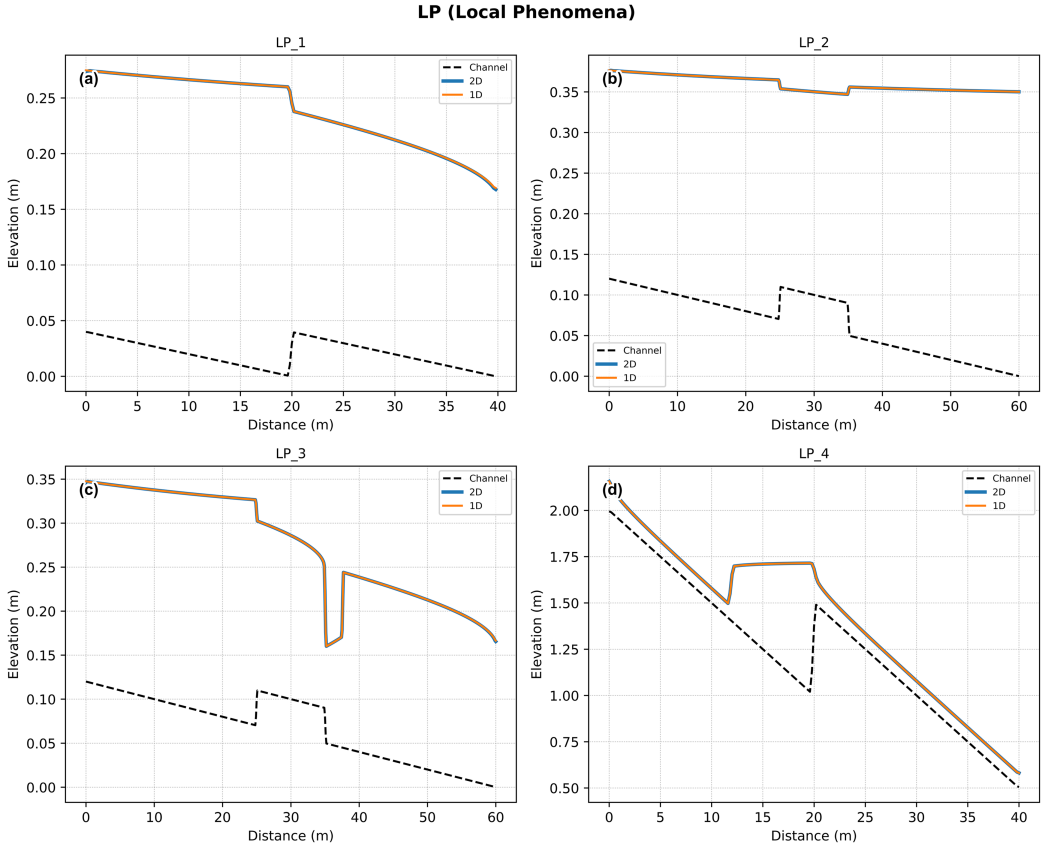


Figure 6: Comparison of 1D and 2D results for local-phenomena IDs LP_1–LP_4. Subfigures depict spatial flow variations for: (**a**) LP_1 Long step; (**b**) LP_2 Short step; (**c**) LP_3; and (**d**) LP_4 Steep step.

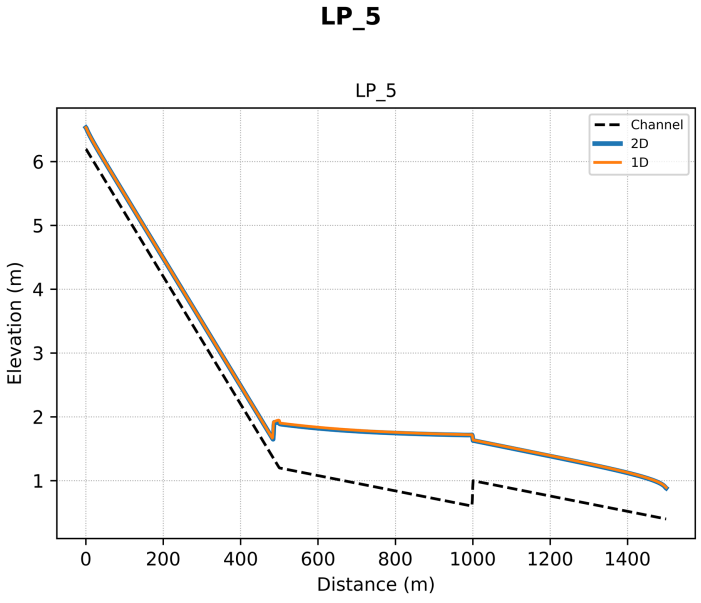


Figure 7: Comparison of 1D and 2D results for local-phenomena ID LP_5.

3.2 Channel Operation Tools

Furthermore, the introduction of common hydraulic structures is validated in Fig. 8. The base geometry of the simulated models consists of a 200 m long rectangular channel with a constant width of 0.5 m, where the bed elevation decreases uniformly from 10 m at the inlet (x = 0 m) to 0 m at the outlet (x = 200 m). Table 4 synthesizes the ID, main characteristics, boundary conditions (BCond), and internal conditions (ICond) of the simulated channel operation tools (COT) models.

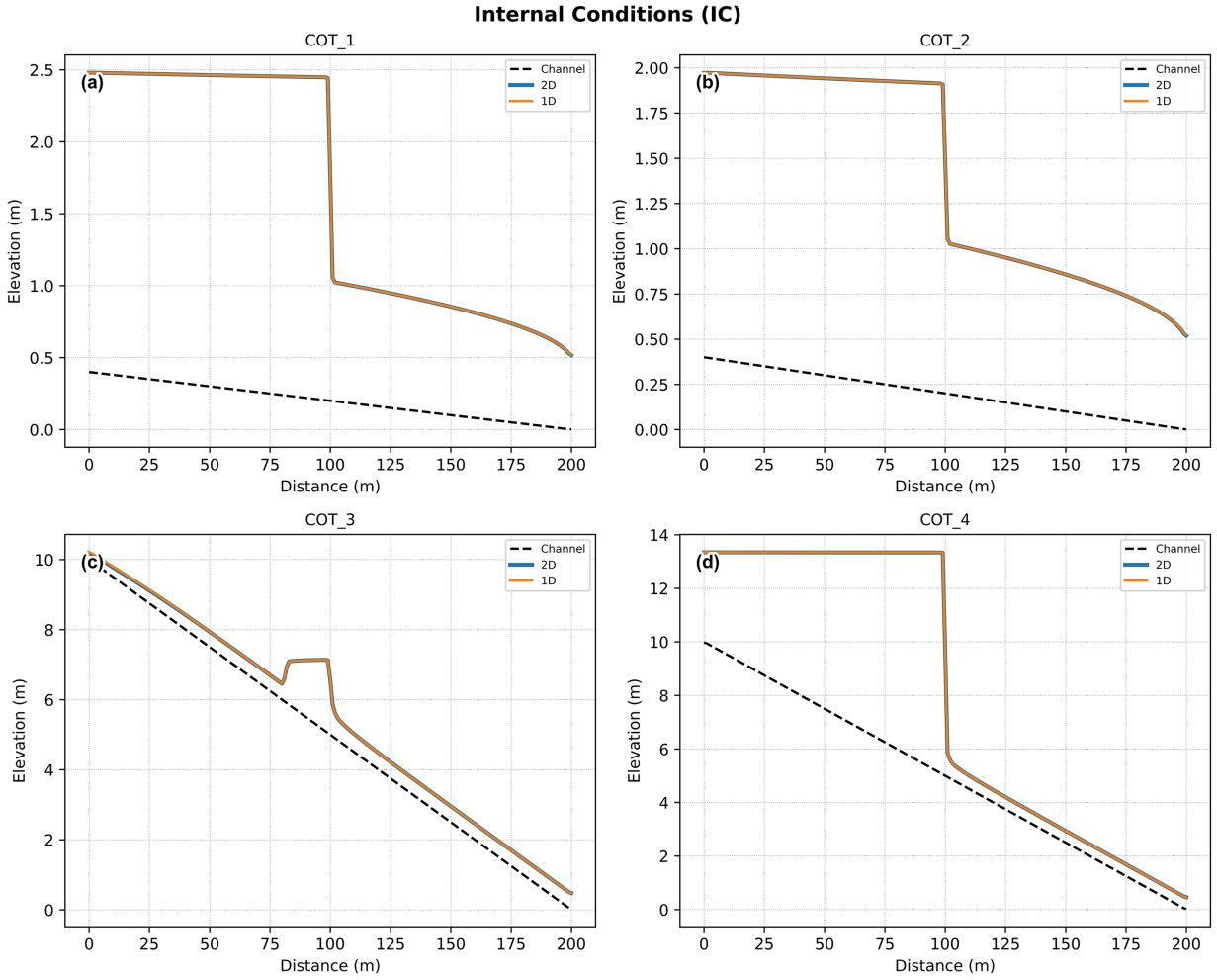


Figure 8: Comparison of 1D and 2D results for internal boundary conditions (gates and weirs) for COT_1 to COT_4 (**a**–**d**).

Table 4: ID, main characteristics, boundary conditions (BCond), and internal conditions (ICond) of the channel operation tools test cases.

ID	Main Characteristics	Inlet BCond	ICond Elev.	Outlet BCond
COT_1	Sluice gate	Subcritical (Q = 0.5 m^3/s)	Gate (z = 0.45 m)	Supercritical

(Continued)

Table 4 (continued)

ID	Main Characteristics	Inlet BCond	ICond Elev.	Outlet BCond
COT_2	Weir	Subcritical (Q = 0.5 m^3/s)	Weir (z = 1.20 m)	Supercritical
COT_3	Sluice gate	Supercritical (Q = 1.0 m^3/s, v = 10 m/s)	Gate (z = 5.25 m)	Supercritical
COT_4	Weir	Supercritical (Q = 1.0 m^3/s, v = 10 m/s)	Weir (z = 6.00 m)	Supercritical

In the case of the sluice gate (COT_1 and COT_3), the model successfully captures the entire mixed-flow sequence. Upstream of the gate, a significant backwater effect creates a pronounced M1 profile. The gate then discharges a high-velocity jet, initiating a supercritical M3 profile downstream. This profile eventually terminates in a hydraulic jump to match the tailwater condition. The model's ability to seamlessly handle the subcritical upstream, the internal boundary condition of the gate, and the supercritical-to-subcritical transition downstream justifies its use for analyzing and operating channels with gate controls.

Similarly, for the weir (COT_2 and COT_4), the model accurately reproduces the M1 backwater profile upstream of the structure caused by the obstruction to flow. The close agreement between the 1D and 2D models validates the implementation of the weir equations within the 1D framework. This confirms the model's reliability for applications involving weirs for flow measurement, water level control, and energy dissipation.

3.3 Channel Network

This section presents the validation of the model using the hypothetical non-looped channel network proposed by Akan and Yen (1981) [54]. This benchmark is of particular importance as it evaluates the model's capability to handle complex interactions between multiple reaches and the mass and momentum transfer through junctions, which are critical components in large-scale irrigation networks. By comparing the 1D model results against a fully hydrodynamic 2D simulation, we can assess the validity of the simplified junction formulations described in Section 2.

3.3.1 Test Case Description

The network configuration consists of two junctions and six channel reaches, as illustrated in Fig. S5 (Supplementary Material). The system is discretized into computational cells with a length of Δx = 10 m.

The geometric and hydraulic properties of the channels are detailed in Table 5. The initial condition is a steady flow state derived from the initial discharges (Q_{ini}) specified in the table, with a corresponding normal depth of 0.6 m established throughout all channels.

3.3.2 Boundary Conditions and Junction Modeling

Unsteady inflow hydrographs are imposed at the upstream inlets of Channels 1, 2, 3, and 5. The shape and timing of these hydrographs are presented in Fig. 9. At the downstream boundary, a constant water depth of 0.6 m is maintained at the outlet of Channel 6.

Table 5: Geometric and hydraulic properties of the channel network.

ID	L [m]	S_0 [-]	B [m]	n [s/m$^{1/3}$]	Q_{ini} [m^3/s]	h_{ini} [m]
1	600	0.0005	5	0.0207	2	0.6
2	600	0.0005	5	0.0207	2	0.6
3	600	0.0005	5	0.0138	3	0.6
4	600	0.0010	8	0.0141	7	0.6
5	600	0.0005	5	0.0138	3	0.6
6	600	0.0010	10	0.0125	10	0.6

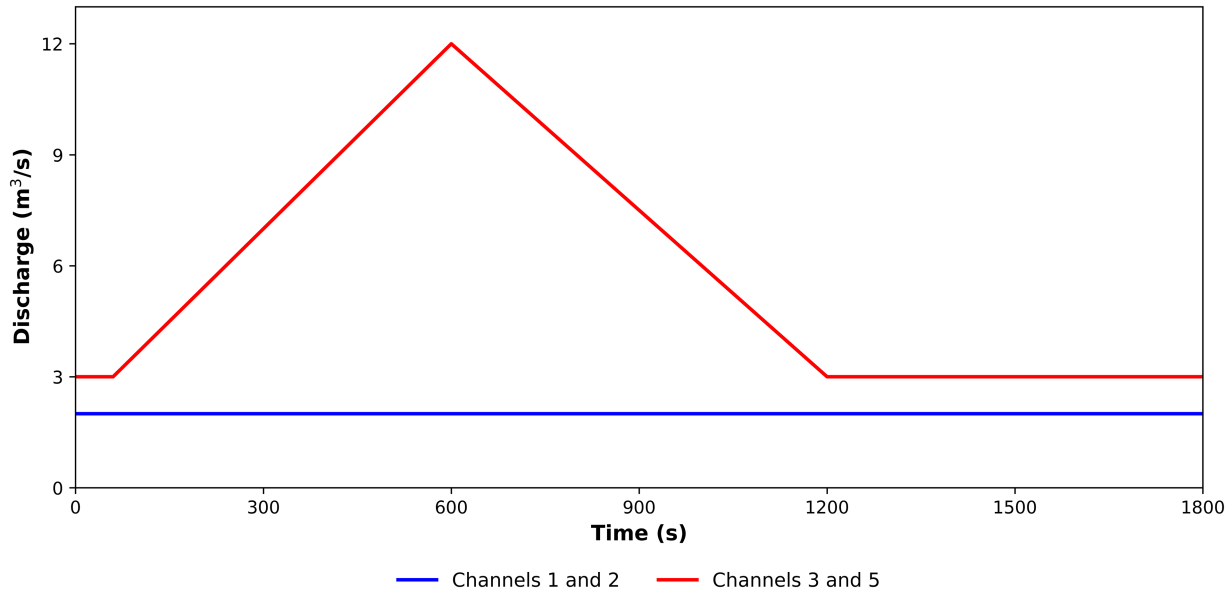


Figure 9: Input hydrographs imposed at the upstream boundary nodes.

The network contains two junctions (Nodes 4 and 6) with a bottom elevation of 0 m. Node 4 has a plan area of 50.265 m^2 and an initial depth of 0.6 m, while Node 6 has an area of 78.540 m^2 and an initial depth of 0.9 m. To validate the results, the 1D model is compared against a 2D reference simulation. In the 2D model, junctions are meshed as rectangular elements (8 m × 6.283 m for Node 4; 10 m × 7.854 m for Node 6) with a Manning's coefficient of 0.010 s/m$^{1/3}$. In contrast, the newly developed 1D model treats these junctions as storage volumes with an equal water surface elevation assumption, as detailed in the mathematical formulation in Section 2.

3.3.3 Results and Analysis

The discharge hydrographs computed by both the 1D and 2D models are compared in Fig. 10. The results indicate a high degree of similarity between the two approaches, confirming the 1D model's ability to propagate water waves through a network structure.

For the upstream branches (Channels 1, 2, 3, and 5), the 1D model (orange line) captures the peak magnitude and timing almost identically to the 2D model (blue line). The rapid variations in discharge, particularly the sharp drops and recoveries observed in Channels 1 and 2, are reproduced with high fidelity.

This suggests that the inlet boundary condition handling and the Roe solver's shock-capturing capabilities are functioning correctly. However, minor discrepancies are observed in the downstream reaches, specifically Channels 4 and 6, which are located immediately after the junctions. In Channel 4, the 1D model predicts a slightly lower peak discharge compared to the 2D model, with a marginally faster recession limb. Similarly, in Channel 6, the peak discharge in the 1D model is slightly attenuated compared to the 2D reference.

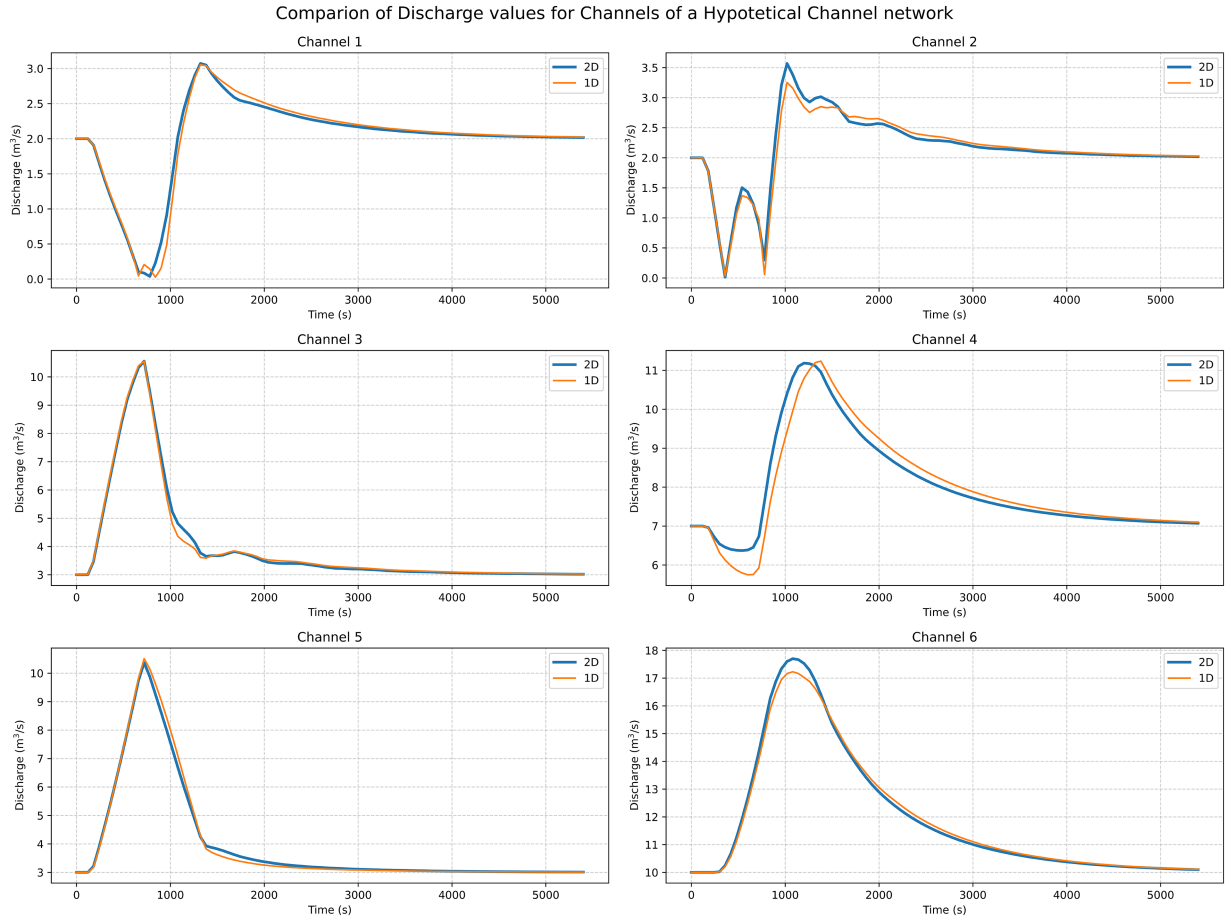


Figure 10: Comparison of discharge hydrographs between the 1D and 2D models.

These differences are attributable to the simplified treatment of junction dynamics in the 1D framework. As described in Section 2, the 1D junction model utilizes a volume-balance approach where the water level is assumed to be horizontal across the junction surface. The 2D model, conversely, solves the full Shallow Water Equations within the junction, allowing for sloping water surfaces, recirculation zones, and complex momentum transfer. The "equal level" assumption in the 1D model essentially implies infinite wave celerity across the junction node, which can lead to slight damping of peak flows and minor phase shifts when high-momentum flows merge, as observed in the transition to Channels 4 and 6.

Despite these minor deviations, the 1D model successfully reproduces the network's macroscopic behavior at significantly reduced computational cost, validating its suitability for operational hydraulics in complex canal systems.

3.4 Street Crossing Network

This section details the validation of the 1D junction formulation using the experimental and numerical data from the "street crossing" test case presented by Blade (2005) [71]. The experimental data were originally obtained by Nania (1999) [72] at the Laboratory of Reduced Models of Universitat Politècncia de Catalunya (UPC), designed to analyze flow distribution in urban intersections. This benchmark is crucial for validating the model's ability to handle flow confluence and bifurcation in orthogonal junctions, a common feature in channel networks and urban drainage systems. Here, the proposed 1D model is compared with spatially averaged results from a rigorous 2D shallow-water simulation.

3.4.1 Test Case Description

The geometry consists of two intersecting channels forming a cross (+) shape, as illustrated in Fig. S6 (Supplementary Material). The setup includes two inlet channels and two outlet channels.

The geometric characteristics are uniform across the intersection. Both channels have a width of $W = 1.5$ m. The two upstream (inlet) reaches have a length of 2.0 m, while the two downstream (outlet) reaches extend for 5.0 m. The channel bottoms are horizontal within the intersection zone, though the incoming and outgoing reaches may have variable slopes depending on the specific experimental run. For the numerical validation presented here, a Manning's roughness coefficient of $n = 0.010$ s/m$^{1/3}$ is applied globally, consistent with the smooth concrete finish of the experimental flume.

3.4.2 Modeling Strategy and Boundary Conditions

In the 1D numerical framework, this domain is discretized into four distinct channel reaches connected to a single central junction node. Discharges are imposed at the upstream boundaries of the North and West arms (Inlets), while free flow conditions or controlled levels are applied at the South and East boundaries (Outlets). The intersection itself is modeled as a storage node with a plan area of 2.25 m^2 (1.5 m × 1.5 m).

The computational mesh is defined consistently for both approaches. The 1D representation uses 126 linear elements (63 for each channel) along the channel centerlines. The 2D reference model discretizes the same domain using 2,116 quadrilateral elements. The characteristic mesh size is approximately 0.10 m, which ensures a nearly uniform spatial resolution across the cross-shaped junction and branch reaches.

3.4.3 Validation Methodology

The validation focuses on the flow properties within the junction itself. While standard 1D models provide a single sequence of variables for the junction node, 2D hydrodynamic models resolve the complex free-surface gradients and recirculation patterns inside the intersection. To ensure a consistent comparison between a 0D nodal outcome and a 2D mesh, the results from the reference 2D simulation (Bladé, 2005) were post-processed by spatially averaging the variables (water depth and velocity components) across the entire confluence area (the central 1.5 × 1.5 m square).

It is critical to acknowledge the inherent limitation of this validation workflow. Comparing the 1D model against "confluence-zone averaged" 2D results evaluates the model's accuracy in predicting the *bulk* macroscopic properties of the junction (i.e., its overall mass and momentum retention and the resulting transfer to the outlet boundaries). It does not, however, validate the model against the complex, resolved 2D flow structures (such as shear layers or recirculation eddies) that exist within the intersection. While this spatially-averaged ground truth confirms the robustness of the storage-volume mass and momentum conservation approach at the network scale, it inherently masks the localized, high-resolution hydrodynamic phenomena that fully 2D models are designed to capture.

3.4.4 Results and Analysis

The predictive capability of the proposed 1D junction formulation is evaluated by comparing the computed hydraulic variables against spatially averaged results from the 2D reference simulation. To rigorously quantify the model performance, the Nash-Sutcliffe Efficiency (NSE) metric is utilized. The NSE is defined as:

$$NSE = 1 - \frac{\sum_{i=1}^{N}(O_i - P_i)^2}{\sum_{i=1}^{N}(O_i - \bar{O})^2} \tag{15}$$

where O_i are the observed (2D reference) values, P_i are the predicted (1D) values, and $\bar{O}$ is the mean of the observed data. An NSE value of 1.0 indicates a perfect match.

The performance of the model across three different slope configurations ($S_x - S_y$: 1%–1%, 1%–2%, and 2%–2%) is summarized in Fig. 11.

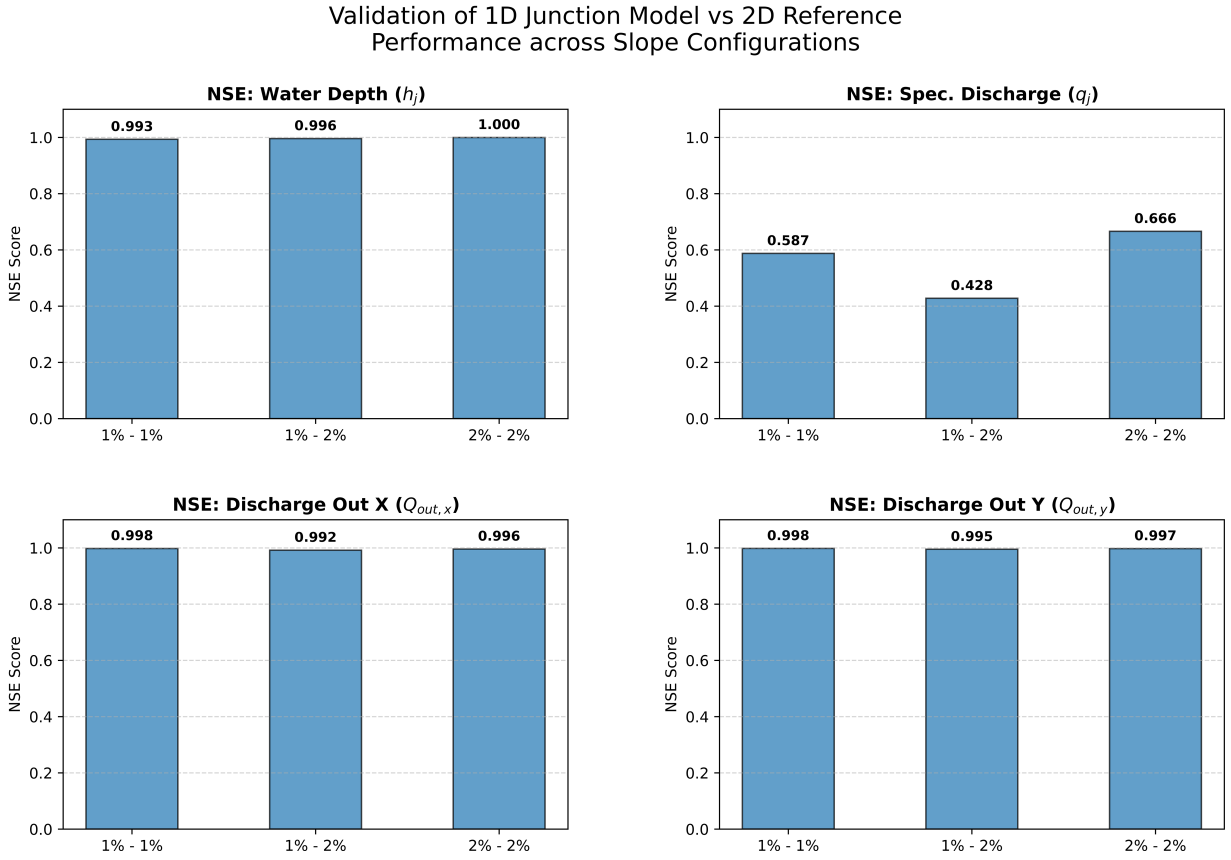


Figure 11: (Continued)

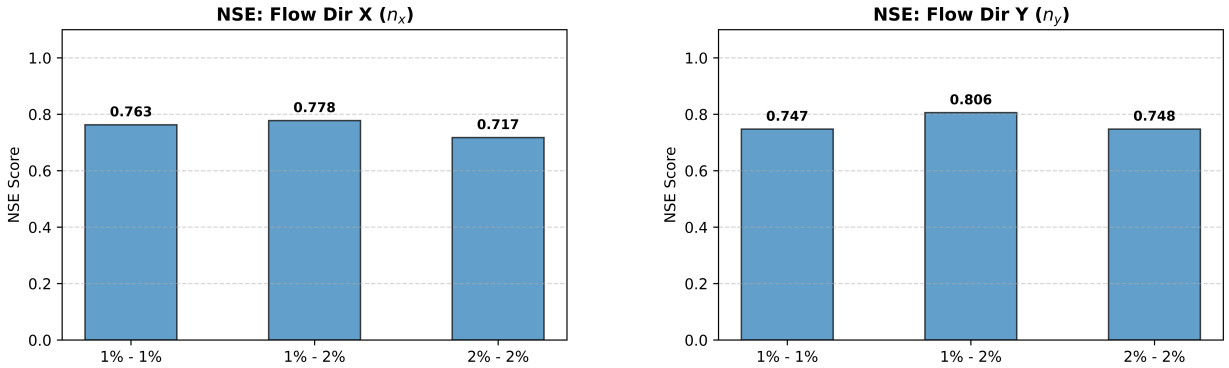


Figure 11: Nash-Sutcliffe Efficiency (NSE) scores for hydraulic variables (water depth, specific discharge, outlet discharges, and flow direction components) across different slope configurations.

The analysis reveals the following performance characteristics:

- **Water Depth (h_j):** The model demonstrates excellent accuracy, with NSE scores consistently exceeding 0.99 for all slope configurations. This confirms that the storage-based continuity equation effectively captures the total mass balance and determines the correct nodal water surface elevation.
- **Outlet Discharge Distribution ($Q_{out,x}, Q_{out,y}$):** Contrary to the specific discharge results, the bulk flow splitting into the outlet branches is predicted with high precision, achieving NSE scores between 0.992 and 0.998. This high performance is directly linked to the accuracy of the water depth (h_j). In the 1D framework, the discharge into an outlet channel is primarily a function of the hydraulic head at the junction node. Since the 1D model correctly predicts the nodal water level, the driving head for the outlet branches is accurate, resulting in correct discharge partitioning. The symmetric configurations (1%–1% and 2%–2%) show nearly perfect agreement ($NSE \approx 0.998$). A very slight reduction is observed in the asymmetric case (1%–2%, with $NSE \approx 0.992$), indicating that while geometric asymmetry introduces complex 2D diffraction effects, the 1D approximation remains robust for routing purposes.
- **Specific Discharge (q_j), and Flow Direction (n_x, n_y):** The specific discharge magnitude (q_j) shows moderate agreement (NSE ≈ 0.43–0.67), while flow direction components perform better (NSE ≈ 0.72–0.81). This highlights a distinction between internal junction variables and boundary fluxes. The 1D model simplifies the complex internal velocity field (averaging the momentum vector), leading to lower scores for q_j. However, this simplification does not propagate errors to the boundaries, as evidenced by the excellent Q_{out} results.

3.4.5 Summary of Limitations and Capabilities

The validation demonstrates that the 1D model is exceptionally reliable for macroscopic variables: water levels and branch discharges. The simplified junction formulation successfully conserves mass and correctly partitions flow based on nodal head, making it ideal for large-scale network modeling. The limitation is confined to the resolution of the internal velocity vector field (q_j) within the junction element itself, which does not negatively impact the routing accuracy for downstream reaches.

4 Discussion

4.1 Channel Network Modelling

The research presented in this study addresses the critical trade-off in hydrodynamic modeling between the computational efficiency of one-dimensional (1D) schemes and the physical accuracy required to simulate complex flow behaviors at channel junctions. While traditional 1D models are indispensable for

simulating large-scale channel networks, they inherently fail to capture the multi-directional flow dynamics, energy dissipation, and momentum transfer that occur where channels converge or diverge. This limitation has historically necessitated the use of empirical coefficients or computationally expensive two-dimensional (2D) models to resolve junction hydraulics [55,56].

The core of the developed methodology lies in its consistent numerical implementation. The 1D channels are solved using the Saint-Venant equations discretized with a first-order Finite Volume Method, employing Roe's approximate Riemann solver to accurately capture shock waves and discontinuities. This is seamlessly coupled to the junction model, which updates the water level and velocity components within the junction based on the flux balance from connecting channels.

4.2 Hydrodynamics and Section Shape

The hydrodynamics are overall well captured. For gradually varied flow, the model accurately reproduced standard backwater curves (M1, M2, M3) and steep-slope profiles (S1, S3), confirming its ability to handle both subcritical and supercritical regimes. Crucially, the model successfully captured rapidly varied flow phenomena, including the formation and location of hydraulic jumps, which are notoriously difficult for traditional schemes to resolve. The validation extended to hydraulic structures, where the model effectively simulated the complex mixed-flow regimes induced by sluice gates and weirs, or by abrupt changes in the channel geometry. While the model demonstrated high precision for macroscopic variables (achieving Nash-Sutcliffe Efficiency scores above 0.99 for water levels and branch discharges in junction tests), the approximation yields moderate agreement (NSE ≈ 0.43–0.67) for the specific discharge immediately within the junction domain. This performance profile proves that the model correctly distributes flow and propagates waves through multiple bifurcations and confluences, prioritizing network routing accuracy over high-resolution localized physics.

To illustrate the localized hydrodynamics at the orthogonal crossing, Fig. 12 maps the detailed 2D water depth and specific discharge. Subplot (a) reveals upstream water accumulation, with depths peaking near 0.125 m and rapidly dropping below 0.025 m in the downstream lateral branches. Subplot (b) highlights a primary diagonal flow corridor reaching specific discharges up to 0.075 m^2/s, contrasting sharply with downstream low-momentum recirculation zones where values fall below 0.015 m^2/s. While the proposed 1D methodology inherently averages out these complex intra-junction gradients by treating the node as a single macroscopic storage volume, it successfully translates the aggregate mass and energy transfer downstream. This demonstrates the 1D model's key advantage: exchanging the computational cost of resolving sub-meter eddies for the high efficiency required in large-scale network applications.

The 1D module of Iber also includes circular and trapezoidal cross-sections. To demonstrate hydrodynamic performance for these geometries, a straight channel was simulated with both the 1D and 2D approaches, using an inlet discharge of 1 m^3/s, a critical/supercritical outlet condition, and a Manning coefficient of $n = 0.015$. The channel slope was set to 0.00175 m/m for the circular section and 0.0175 m/m for the trapezoidal section. In both cases, the channel length was selected to ensure steady conditions without boundary-condition interactions.

The numerical results from both approaches were compared with the analytical solution based on Manning's equation for a circular section with diameter $D = 6$ m and a trapezoidal section with bottom and top widths of 1 and 3 m, respectively. Table 6 summarizes the hydraulic variables, showing good agreement between numerical and analytical results. Both numerical approaches provide a close fit, while the small differences in the 2D simulations are attributed to geometric discretization: flow–boundary interactions and the associated energy dissipation are computed element by element, rather than over the full wetted section as in the 1D approach.

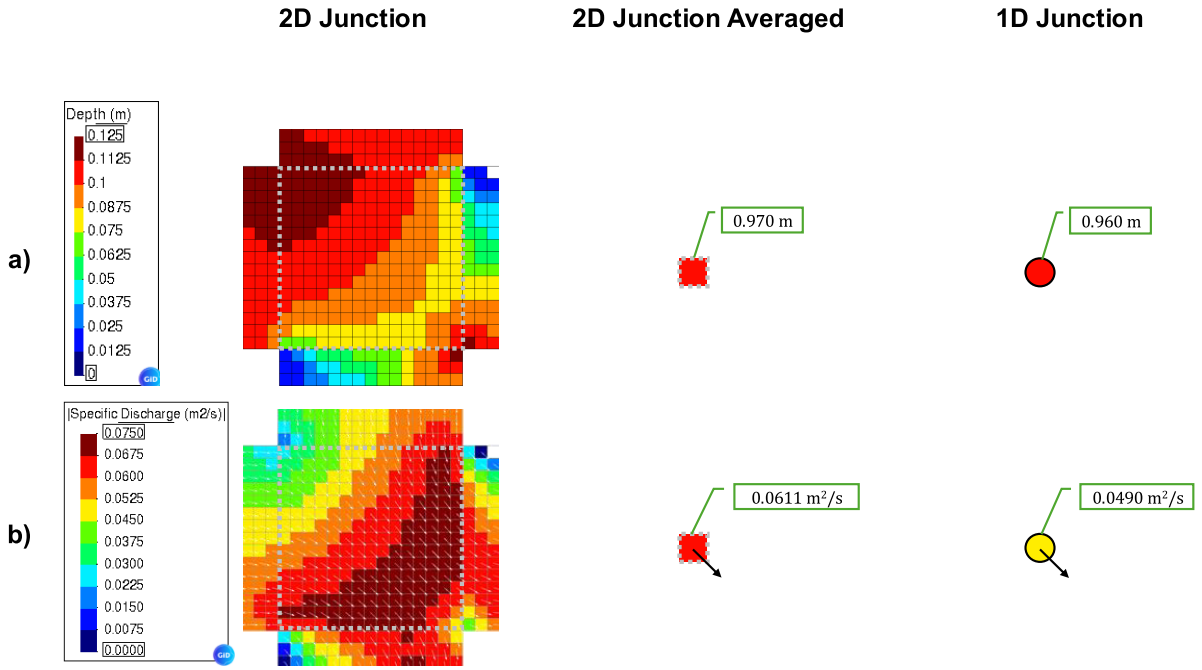


Figure 12: Detailed 2D hydrodynamic flow fields at the orthogonal street crossing. Subplot (**a**) maps localized water depths, highlighting upstream accumulation peaking near 0.125 m. Subplot (**b**) depicts specific discharge and flow vectors, showing a primary flow path up to 0.075 m^2/s alongside low-momentum recirculation zones. The 1D network model replaces these localized gradients with an efficient volume-balance approach.

Table 6: Hydraulic comparison for circular and trapezoidal sections (1D, 2D, and analytical solutions).

Shape	Depth (m)	Wet Perimeter (m)	Top Wet Width (m)	Wet Area (m^2)
Circular (1D)	0.411	3.195	3.032	0.843
Circular (2D)	0.391	2.962	3.095	0.784
Analytical (circ.)	0.418	3.200	3.044	0.861
Trapezoidal (1D)	0.268	1.757	1.535	0.340
Trapezoidal (2D)	0.250	1.707	1.480	0.310
Analytical (trap.)	0.268	1.757	1.535	0.340

4.3 Performance

This section analyses the numerical performance of the new 1D approach in comparison with the 2D solution used as a reference for hydrodynamic purposes. The observed computational speed-up is fundamentally driven by two factors. First, for standard straight channels where the number of computational elements is comparable between both approaches, the 1D model is inherently faster because it solves a reduced set of governing equations per element compared to the full 2D shallow-water equations. Second, in complex configurations involving junctions or abrupt width variations, the 2D approach requires a significantly higher element density to resolve local flow features. In these cases, the 1D approach maintains its efficiency by computing a unified macroscopic mass and momentum balance for the entire junction volume, completely bypassing the need for a high-density internal computational mesh. The speed-up was calculated as the quotient between the computing time of the 2D approach and the 1D approach. Fig. S7 (Supplementary

Material) summarizes the results, dividing the test cases into a 2 × 2 grid categorized by their specific hydrodynamics and network configurations.

Test cases based on a straight channel, in which the computational domain was discretized with the same number of elements in both approaches, consistently exhibited a speed-up between 2.10 and 3.57. As illustrated in Fig. S7 (Supplementary Material), these base cases span across the Gradually Varied Flow (GVF), the combined Gradually and Rapidly Varied Flow (GVF/RVF), and the standard Local Phenomenon (LP) test cases.

An outlier within the straight channels is test case LP_5. Despite being a straight channel, the section width reduction at the end of the first third of the channel implied the utilization of a significantly greater number of elements in the 2D approach (13,000 surface elements vs. 1500 line elements). In such a case, the speed-up spiked to 13.16 due to the larger element count and the inherent performance advantages of the 1D model over the 2D.

A similar, yet more pronounced behavior was observed for the complex network configurations. As shown in the Channel Networks subplot, the standard channel network (CN) and the street crossing models (ST 1%–1%, ST 1%–2%, and ST 2%–2%) yielded massive speed-ups ranging from 15 to over 22 times. The independent vertical scales in Fig. S7 (Supplementary Material) clearly highlight this distinct performance bracket compared to the standard straight-channel flows.

These results highlight not only a notable improvement in terms of computing time for the 1D approach in standard straight channels (averaging a 2.5-times speed-up), but also the substantial benefits of employing a 1D approach in varying geometrical situations, with or without junctions. This is especially advantageous in scenarios where the detailed 2D hydrodynamics within a junction are not the primary subject of study.

Overall, this evidence underscores the significant contribution of this research: a computationally efficient tool that does not compromise on physical realism where it matters most. The ability to simulate complex networks with the accuracy of a 2D model at junctions but at a fraction of the computational cost represents a major advancement for operational flood forecasting and the management of extensive irrigation systems. However, the current implementation is not without limitations. The use of an explicit time integration scheme imposes a strict constraint on the time step via the CFL condition, which can impact simulation times for very fine meshes. Additionally, while the junction model captures the bulk 2D effects, it does not resolve the detailed internal velocity distribution, which may be relevant for localized sediment transport studies.

4.4 Beyond Current Implementation

Future research lines will focus on addressing these limitations and expanding the model's capabilities. A primary objective is the implementation of an implicit or semi-implicit time stepping scheme to relax the stability constraints and further accelerate simulations. To enhance the model's applicability to comprehensive flood risk management, future work will also involve coupling the current 1D network model with a 2D floodplain module, creating a fully integrated 1D-2D system. Finally, the modular nature of the finite volume framework allows for the incorporation of transport equations, opening the door to simulating sediment transport and water quality dynamics within the same efficient computational structure.

5 Conclusions

This work has developed and validated a novel hybrid hydrodynamic model, based on Iber, that integrates a robust 1D finite volume solver for channel reaches with a physics-based 2D coupling formulation for junctions. The proposed methodology treats the junction not as a simple point node, but as a storage

volume where mass and momentum are rigorously conserved, allowing for the simulation of complex flow patterns without relying on regime-dependent empirical parameters. By treating the junction variables as a 2D flow field and applying Roe's flux difference splitting at the interfaces, the model effectively resolves the "scale mismatch" problem. This approach ensures that the macroscopic 2D momentum transfer and associated head losses are inherently captured in the junction's mass and momentum balance, bypassing the need for regime-specific empirical factors, while the rest of the network benefits from the speed of the 1D solution.

The validation of the proposed model was conducted through a rigorous comparative analysis against a well-established 2D shallow water model (Iber), covering a comprehensive range of flow conditions and geometric configurations, both in straight channels and channel networks. The quantitative benchmarking demonstrated robust performance for all macroscopic variables. In junction and network scenarios, the 1D model achieved excellent agreement (NSE > 0.99) with the spatially-averaged 2D reference for water depths and boundary discharges. However, as expected for a simplified control-volume approach, agreement was moderate (NSE 0.43–0.67) for internal velocity vectors. These findings confirm the model's suitability for large-scale network routing and operational hydrology, where bulk mass and momentum transfer govern the flow distribution. The primary limitations of the current framework are its inability to resolve complex, localized 2D hydrodynamics (such as recirculation eddies) within the junction volumes and the strict time-step constraints imposed by the explicit integration scheme via the CFL condition.

Acknowledgement: Not applicable.

Funding Statement: This study is commissioned by the Water Catalan Agency (Agència Catalana de l'Aigua-ACA) and funded by the Next Generation EU initiative. The project is part of the environmental restoration efforts of the Ebro River and its Delta. It is aligned with Investment 2 of Component 5 of the Spanish Government's Restoration, Transformation, and Resilience Plan. It contributes to achieving the objectives outlined in the CID 77 milestone, Restoration of Riverbed and Bank Protection against Flood Risks.

Author Contributions: The authors confirm contribution to the paper as follows: Conceptualization, Danial Dehghan-Souraki and Marcos Sanz-Ramos; methodology, Marcos Sanz-Ramos; software, Danial Dehghan-Souraki; validation, Danial Dehghan-Souraki, Marcos Sanz-Ramos and Ernest Bladé i Castellet; formal analysis, Danial Dehghan-Souraki; investigation, Danial Dehghan-Souraki; resources, Marcos Sanz-Ramos; data curation, Marcos Sanz-Ramos; writing—original draft preparation, Danial Dehghan-Souraki; writing—review and editing, Marcos Sanz-Ramos and Ernest Bladé i Castellet; visualization, Danial Dehghan-Souraki; supervision, Ernest Bladé i Castellet; project administration, Marcos Sanz-Ramos; funding acquisition, Ernest Bladé i Castellet. All authors reviewed and approved the final version of the manuscript.

Availability of Data and Materials: The data that support the findings of this study are available from the Corresponding Author, D.D.S., upon reasonable request.

Ethics Approval: Not applicable.

Conflicts of Interest: The authors declare no conflicts of interest.

Supplementary Materials: The supplementary material is available online at https://www.techscience.com/doi/10.32604/rimni.2026.082533/s1.

Abbreviations

The following abbreviations are used in this manuscript:

1D	One-Dimensional
2D	Two-Dimensional
ACA	Agència Catalana de l'Aigua (Water Catalan Agency)
CID	Council Implementing Decision
CIMNE	International Center for Numerical Methods in Engineering
CFL	Courant–Friedrichs–Lewy
CN	Channel Network
COT	Channel Operation Tools
CSO	Combined Sewer Overflow
DEM	Digital Elevation Model
FVM	Finite Volume Method
GEAMA	Group of Water and Environmental Engineering
GVF	Gradually Varied Flow
JRP	Junction Riemann Problem
LP	Local Phenomenon
NSE	Nash–Sutcliffe Efficiency
RVF	Rapidly Varied Flow
ST	Street Crossing Test Case
SWE	Shallow Water Equation
UPC	Universitat Politècnica de Catalunya

References

1. Löwe R, Urich C, Domingo NS, Mark O, Deletic A, Arnbjerg-Nielsen K. Assessment of Urban pluvial flood risk and efficiency of adaptation options through simulations—a new generation of urban planning tools. J Hydrol. 2017;550:355–67. doi:10.1016/j.jhydrol.2017.05.009.
2. Mojaddadi H, Pradhan B, Nampak H, Ahmad N, Ghazali AH. Ensemble machine-learning-based geospatial approach for flood risk assessment using multi-sensor remote-sensing data and GIS. Geomat, Nat Hazards Risk. 2017;8:1080–102.
3. Rosenzweig BR, Herreros Cantis P, Kim Y, Cohn A, Grove K, Brock J, et al. The value of Urban flood modeling. Earth's Future. 2021;9(1):e2020EF001739. doi:10.1029/2020ef001739.
4. Castelletti A, Ficchì A, Cominola A, Segovia P, Giuliani M, Wu W, et al. Model predictive control of water resources systems: a review and research agenda. Annual Rev Control. 2023;55:442–65. doi:10.1016/j.arcontrol.2023.03.013.
5. Tahiri A, Che D, Ladeveze D, Chiron P, Archimède B. Network flow and flood routing model for water resources optimization. Sci Rep. 2021;12:3937. doi:10.21203/rs.3.rs-914804/v1.
6. Loucks DP. Hydroinformatics: a review and future outlook. Camb Prism Water. 2023;1:e10.
7. Walsh CJ, Roy AH, Feminella JW, Cottingham PD, Groffman PM, Morgan RP. The urban stream syndrome: current knowledge and the search for a cure. J N Am Benthol Soc. 2005;24(3):706–23. doi:10.1899/04-028.1.
8. Fletcher TD, Andrieu H, Hamel P. Understanding, management and modelling of urban hydrology and its consequences for receiving waters: a state of the art. Adv Water Resour. 2013;51:261–79. doi:10.1016/j.advwatres.2012.09.001.
9. Hassan BT, Yassine M, Amin D. Comparison of urbanization, climate change, and drainage design impacts on urban flashfloods in an arid region: case study, New Cairo, Egypt. Water. 2022;14(15):2430.
10. Graf W. Network characteristics in suburbanizing streams. Water Resour Res. 1977;13:459–63. doi:10.1029/wr013i002p00459.
11. Khan ST, Sample D, Wynn-Thompson T, Butcher JB. Impacts of climate change on storm event-based flow regime and channel stability of urban headwater streams. J Environ Manage. 2025;374:123994. doi:10.1016/j.jenvman.2024.123994.

12. Miller J, Hutchins M. The impacts of urbanisation and climate change on urban flooding and urban water quality: a review of the evidence concerning the United Kingdom. J Hydrol Reg Studies. 2017;12:345–62. doi:10.1016/j.ejrh.2017.06.006.
13. Sañudo E, Cea L, Puertas J. Modelling pluvial flooding in urban areas coupling the models Iber and SWMM. Water. 2020;12(9):2647. doi:10.3390/w12092647.
14. Montalvo C, Reyes-Silva JD, Sañudo E, Cea L, Puertas J. Urban pluvial flood modelling in the absence of sewer drainage network data: a physics-based approach. J Hydrol. 2024;634:131043. doi:10.1016/j.jhydrol.2024.131043.
15. Schmitt T, Thomas M, Ettrich N. Analysis and modeling of flooding in urban drainage systems. J Hydrol. 2004;299:300–11. doi:10.1016/s0022-1694(04)00374-9.
16. Bermúdez M, Ntegeka V, Wolfs V, Willems P. Development and comparison of two fast surrogate models for urban pluvial flood simulations. Water Resour Manag. 2018;32:2801–15. doi:10.1007/s11269-018-1959-8.
17. Aragón Hernández JL, Bladé E. Modelación numérica de flujo mixto en conductos cerrados con esquemas en volúmenes finitos. Tecnología Y Ciencias Del Agua. 2017;8(3):127–42. doi:10.24850/j-tyca-2017-03-08.
18. Sun L, Dai S, Tian L, Ni Z, Lu S, Yao Y. Optimal water allocation considering water diversion projects in an agricultural irrigation district. Agriculture. 2025;15(9):949. doi:10.3390/agriculture15090949.
19. Yao L, lou Li Y, Chen X. A robust water-food-land nexus optimization model for sustainable agricultural development in the Yangtze River Basin. Agric Water Manag. 2021;256:107103. doi:10.1016/j.agwat.2021.107103.
20. Gumiere S, Bissonnais YL, Raclot D, Cheviron B. Vegetated filter effects on sedimentological connectivity of agricultural catchments in erosion modelling: a review. Earth Surface Processes Landforms. 2011;36(1):3–19. doi:10.1002/esp.2042.
21. Lee S, Chu M, Guzman J, Flanagan D, Moriasi D, Fortuna A, et al. Integrated modeling for simulating sediment production and transport in agricultural landscapes. Environ Model Softw. 2022;160:105605. doi:10.1016/j.envsoft.2022.105605.
22. Lebon N, Dagès C, Burger-Leenhardt D, Molénat J. A new agro-hydrological catchment model to assess the cumulative impact of small reservoirs. Environ Model Softw. 2022;153:105409. doi:10.1016/j.envsoft.2022.105409.
23. Shan Y, Zhao T, Liu C, Nepf H. Turbulence and bed load transport in channels with randomly distributed emergent patches of model vegetation. Geophys Res Lett. 2020;47(12):e2020GL087055. doi:10.1029/2020gl087055.
24. Habets F, Molénat J, Carluer N, Douez O, Leenhardt D. The cumulative impacts of small reservoirs on hydrology: a review. Sci Total Environ. 2018;643:850–67. doi:10.1016/j.scitotenv.2018.06.188.
25. Soler Guitart J, Gómez Valentín M, Rodellar Benedé J. Estudio hidráulico para el plan de emergencia del canal de la margen izquierda del Delta del Ebro. Ingeniería Del Agua. 2010;17(2):171–86. doi:10.4995/ia.2010.2975.
26. Lim M, Ginting BM, Senjaya T, Kieswanti C. Comparison of 1D, coupled 1D–2D, and 2D shallow water numerical modeling for dam-break flow analysis of Way-Ela dam, Indonesia. Indones Acta Hydrotech. 2024;37(66):27–50. doi:10.15292/acta.hydro.2024.02.
27. Ishikawa M, Gonzalez W, Golyjeswski O, Sales G, Rigotti JA, Bleninger T, et al. Effects of dimensionality on the performance of hydrodynamic models for stratified lakes and reservoirs. Geosci Model Develop. 2022;15:2197–220. doi:10.5194/gmd-15-2197-2022.
28. Bürgler M, Vetsch D, Boes R, Vanzo D. Systematic comparison of 1D and 2D hydrodynamic models for the assessment of hydropeaking alterations. River Res Appl. 2022;39:460–77. doi:10.1002/rra.4051.
29. Yarodji MAK, Badé R, Saley B. Study of the 1D Saint-venant equations and application to the simulation of a flood problem. J Appl Math Phys. 2020;8(7):1193–206. doi:10.4236/jamp.2020.87090.
30. Yu CW, Hodges BR, Liu F. A new form of the Saint-Venant equations for variable topography. Hydrol Earth Syst Sci. 2020;24(8):4001–24. doi:10.5194/hess-2020-75.
31. Hodges BR. Conservative finite-volume forms of the Saint-Venant equations for hydrology and urban drainage. Hydrol Earth Syst Sci. 2019;23:1281–304. doi:10.5194/hess-2018-242.
32. Barneveld H, Mosselman E, Chavarrías V, Chavarrías V, Hoitink A. Accuracy assessment of numerical morphological models based on reduced Saint-Venant equations. Water Resour Res. 2024;60:e2023WR035052. doi:10.1029/2023wr035052.

33. Saleh F, Ducharne A, Flipo N, Oudin L, Ledoux E. Impact of river bed morphology on discharge and water levels simulated by a 1D Saint-Venant hydraulic model at regional scale. J Hydrol. 2013;476:169–77. doi:10.1016/j.jhydrol.2012.10.027.
34. Pandey R, Jayanth GR, Mohan Kumar MS. Comprehensive mathematical model for efficient and robust control of irrigation canals. Environ Model Softw. 2024;178:106083. doi:10.1016/j.envsoft.2024.106083.
35. Júnior MNG, Rápalo L, Oliveira PTS, Giacomoni M, Lago CD, Mendiondo E. Modeling unsteady and steady 1D hydrodynamics under different hydraulic conceptualizations: model/Software development and case studies. Environ Model Softw. 2023;167:105733.
36. Brunner G. HEC-RAS 2D User's Manual. US Army Corps of Engineers. 2021 [cited 2026 May 20]. Available from: https://www.hec.usace.army.mil/confluence/rasdocs/r2dum/latest.
37. Bladé E, Cea L, Corestein G, Escolano E, Puertas J, Vázquez-Cendón E, et al. Iber: a numerical simulation tool for river flow. Revista Internacional de Métodos Numéricos para Cálculo y Diseño en Ingeniería. 2014;30(1):1–10.
38. Bates P, Horritt M, Fewtrell T. A simple inertial formulation of the shallow water equations for efficient two-dimensional flood inundation modelling. J Hydrol. 2010;387:33–45. doi:10.1016/j.jhydrol.2010.03.027.
39. Mignot E, Paquier A, Haider S. Modeling floods in a dense urban area using 2D shallow water equations. J Hydrol. 2006;327:186–99. doi:10.1016/j.jhydrol.2005.11.026.
40. Dewals B, Kitsikoudis V, Mejía-Morales MA, Archambeau P, Mignot E, Proust S, et al. Can the 2D shallow water equations model flow intrusion into buildings during urban floods? J Hydrol. 2023;619:129231. doi:10.1016/j.jhydrol.2023.129231.
41. Passalacqua P, Belmont P, Staley DM, Simley JD, Arrowsmith JR, Bode CA, et al. Analyzing high resolution topography for advancing the understanding of mass and energy transfer through landscapes: a review. Earth-Sci Rev. 2015;148:174–93. doi:10.1016/j.earscirev.2015.05.012.
42. Kinzel PJ, Legleiter CJ. sUAS-based remote sensing of river discharge using thermal particle image velocimetry and bathymetric lidar. Remote Sens. 2019;11(19):2317. doi:10.3390/rs11192317.
43. Pujol L, Garambois P, Monnier J. Multi-dimensional hydrological-hydraulic model with variational data assimilation for river networks and floodplains. Geosci Model Develop. 2022;15:6085–113. doi:10.5194/egusphere-2022-10.
44. Samarasinghe JT, Basnayaka V, Gunathilake M, Azamathulla H, Rathnayake U. Comparing combined 1D/2D and 2D hydraulic simulations using high-resolution topographic data: examples from Sri Lanka—Lower Kelani River Basin. Hydrology. 2022;9(2):39.
45. Bladé E, Gómez-Valentín M, Dolz J, Aragón-Hernández JL, Corestein G, Sánchez-Juny M. Integration of 1D and 2D finite volume schemes for computations of water flow in natural channels. Adv Water Resour. 2012;42:17–29. doi:10.1016/j.advwatres.2012.03.021.
46. Simon CA, Langendoen EJ, Abad JD, Mendoza A. On the governing equations for horizontal and vertical coupling of one- and two-dimensional open channel flow models. J Hydraulic Res. 2020;58(5):709–24. doi:10.1080/00221686.2019.1671507.
47. Bellamoli F, Müller LO, Toro E. A numerical method for junctions in networks of shallow-water channels. Appl Math Comput. 2017;337:190–213. doi:10.1016/j.amc.2018.05.034.
48. Ghostine R, Ghostine R, Kesserwani G, Mosé R, Vazquez J, Ghenaim A, et al. A confrontation of 1D and 2D RKDG numerical simulation of transitional flow at open-channel junction. Int J Numer Methods Fluids. 2009;61(7):752–67.
49. Lewis Q, Rhoads B, Sukhodolov A, Constantinescu G. Advective lateral transport of streamwise momentum governs mixing at small river confluences. Water Resour Res. 2020;56(9):e2019WR026817. doi:10.1029/2019wr026817.
50. Sukhodolov A, Shumilova O, Constantinescu G, Lewis Q, Rhoads B. Mixing dynamics at river confluences governed by intermodal behaviour. Nat Geosci. 2022;16:89–93. doi:10.1038/s41561-022-01091-1.
51. Constantinescu G, Miyawaki S, Rhoads B, Sukhodolov A, Kirkil G. Structure of turbulent flow at a river confluence with momentum and velocity ratios close to 1: insight provided by an eddy-resolving numerical simulation. Water Resour Res. 2011;47(5):W05507. doi:10.1029/2010wr010018.

52. López-Gómez D, Gassó-Sánchez Á. La turbulencia en canales abiertos. Un enfoque lagrangiano. Ingeniería Del Agua. 2025;29(3):202–12. doi:10.4995/ia.2025.23538.
53. Colombo RM, Garavello M. On the 1D modeling of fluid flowing through a junction. Discrete Contin Dyn Syst-B. 2020;25(10):3917–29. doi:10.3934/dcdsb.2019149.
54. Akan AO, Yen BC. Diffusion-wave flood routing in channel networks. J Hydraul Div. 1981;107(6):719–32. doi:10.1061/jyceaj.0005681.
55. Soler Guitart J, Gómez Valentín M, Rodellar Benedé J. Una herramienta de control de transitorios en canales de regadío. Ingeniería Del Agua. 2004;11(3):297–313. doi:10.4995/ia.2004.2539.
56. Salaheldin TM, Imran J, Chaudhry MH. Simulación de flujos en canales abiertos con pendientes fuertes. Ingeniería Del Agua. 2000;7(4):391–408. doi:10.4995/ia.2000.2854.
57. Elshobaki M, Valiani A, Caleffi V. Numerical modelling of open channel junctions using the Riemann problem approach. J Hydraul Res. 2018;57:662–74.
58. Li Q, Liang Q, Xia X. A novel 1D-2D coupled model for hydrodynamic simulation of flows in drainage networks. Adv Water Resour. 2020;137:103519.
59. Cunge JA, Holly FM, Verwey A. Practical aspects of computational river hydraulics. Boston, MA, USA: Pitman Advanced Pub. Program; 1980.
60. Chow VT. Open-channel hydraulics. McGraw-Hill. 1959 [cited 2026 May 20]. Available from: https://archive.org/details/openchannelhydra0000chow.
61. Toro EF. Riemann solvers and numerical methods for fluid dynamics: a practical introduction. Cham, Switzerland: Springer Science & Business Media; 2009.
62. Villemonte JR. Submerged weir discharge studies. Eng News Record. 1947;139(26):866–9.
63. Cea L, Bladé E, Sanz-Ramos M, Fraga I, Sañudo E, García-Feal O, et al. Benchmarking of the Iber capabilities for 2D free surface flow modelling. 2020 [cited 2026 May 20]. Available from: https://ruc.udc.es/entities/publication/b9a62a6a-ffaf-49aa-aaa0-81f04fe26240.
64. Gómez LC, Pita MB, Areán BS. Cálculo de curvas de remanso y fenómenos locales con Iber. Universidade da Coruña. 2018 [cited 2026 May 20]. Available from: https://ruc.udc.es/bitstreams/398eac40-8552-420e-b474-95e2175fc2bd/download.
65. Cea L, Pena L, Puertas J, Vázquez-Cendón ME, Peña E. Application of several depth-averaged turbulence models to simulate flow in vertical slot fishways. J Hydraul Eng. 2007;133(2):160–72. doi:10.1061/(asce)0733-9429(2007)133:2(160).
66. Sanz-Ramos M, López-Gómez D, Bladé E, Dehghan-Souraki D. A CUDA Fortran GPU-parallelised hydrodynamic tool for high-resolution and long-term eco-hydraulic modelling. Environ Modell Softw. 2023;161:105628. doi:10.1016/j.envsoft.2023.105628.
67. Sanz-Ramos M, Olivares G, Bladé E. Experimental characterization and two-dimensional hydraulic-hydrologic modelling of the infiltration process through permeable pavements. Rev Int Métodos Numér Cálc Diseño Ing. 2022;38(1):14. doi:10.23967/j.rimni.2022.03.012.
68. Innocenti L, Bladé E, Sanz-Ramos M, Ruiz-Villanueva V, Solari L, Aberle J. Two-dimensional numerical modeling of large wood transport in bended channels considering secondary current effects. Water Resour Res. 2023;59(12):e2022WR034363. doi:10.1029/2022wr034363.
69. Chanson H. The hydraulics of open channel flow: an introduction. 2nd ed. Oxford, UK: Elsevier Butterworth-Heinemann; 2004.
70. Valiani A, Caleffi V, Zanni A. Case study: malpasset dam-break simulation using a two-dimensional finite volume method. J Hydraul Eng. 2002;128(5):460–72. doi:10.1061/(asce)0733-9429(2002)128:5(460).
71. Blade E. Modelación del flujo en lámina libre sobre cauces naturales. Análisis integrado con esquemas en volúmenes finitos en una y dos dimensiones. 2005 [cited 2026 May 20]. Available from: https://hdl.handle.net/2117/93706.
72. Nania LS. Metodología numérico-experimental para el análisis del riesgo asociado a la escorrentía pluvial en una red de calles. 1999 [cited 2026 May 20]. Available from: https://hdl.handle.net/2117/93707.